Physicochem. Probl. Miner. Process., 62(6), 2026, 242520

http://www.journalssystem.com/ppmp

Physicochemical Problems of Mineral Processing

ISSN 1643-1049
© Wroclaw University of Science and Technology

Multi-criteria optimization and classification performance of an overflow-adjustable hydrocyclone

Xiaoyu Li [1], Xuepeng Yu [1], Qingxia Meng [2], Anjun Li [1], Peikun Liu [1], Ziqiang Hu [2], Yuekan Zhang [1]

[1.] College of Mechanical and Electronic Engineering, Shandong University of Science and Technology, 266590, Shandong, China

[2.] Naipu Mining Machinery Co., Ltd, 334199, Jiangxi, China

Corresponding author: lianjun@sdust.edu.cn (Anjun Li)

Abstract: To support parameter adjustment of an overflow-adjustable hydrocyclone under changing feed conditions, this study evaluated its classification performance and multi-criteria optimization under a range of steady-state operating conditions. Single-factor experiments quantified the effects of feed concentration, feed pressure, and overflow-baffle height on key classification metrics. Among the variables examined, feed concentration produced the largest observed change in overflow fineness. Increasing the feed solids concentration from 28.5% to 51.9% decreased overflow fineness and classification efficiency by 18.34 and 8.35 percentage points, to 77.27% and 55.21%, respectively. To optimize the conflicting responses of overflow fineness, classification efficiency, and underflow yield simultaneously, an orthogonal design was combined with weighted grey relational analysis. Among the original orthogonal runs, $A_3B_3C_3$ (feed pressure 0.16 MPa, baffle diameter 115 mm, and baffle height 260 mm) produced the highest grey relational grade. Main-effect analysis, however, identified $A_1B_3C_3$ (feed pressure 0.12 MPa, baffle diameter 115 mm, and baffle height 260 mm) as the preferred factor-level combination. A confirmation experiment at $A_1B_3C_3$ yielded an underflow yield of 58.62%, an overflow fineness of 88.91%, and a classification efficiency of 61.05%. Under the specified weights, $A_1B_3C_3$ achieved the highest grey relational grade of 0.8040 among the evaluated conditions and was therefore selected as the preferred multi-response condition. These steady-state comparisons provide a basis for selecting OAHC operating and structural parameters after feed conditions change; transient adjustment performance under continuous fluctuations remains to be evaluated.

Keywords: classification performance, grey relational analysis, hydrocyclone, overflow-adjustable

1. Introduction

Grinding circuits commonly rely on hydrocyclones to separate particles because these units accommodate large slurry throughputs without complex mechanical components and generally require modest operating expenditure (Tian et al., 2018). In industrial operation, variations in ore properties, instability in the grinding process, and fluctuations in the circulating load (Giglia and Aldrich, 2020) often cause changes in the feed concentration of hydrocyclones (Kuang et al., 2012; Zhang et al., 2024). Such variations may disturb the normal partitioning of particles between the two product streams: coarse particles can enter the overflow (Zhao et al., 2021), whereas fine particles can report to the underflow (Padhi et al., 2021), thereby impairing classification efficiency (Kumar et al., 2021) and adversely affecting downstream separation, increasing equipment wear, and imposing a greater operating load (Zhang et al., 2011). Therefore, clarifying hydrocyclone classification behavior under varying feed conditions has become an important research topic in grinding-classification systems (Endres et al., 2012).

The vortex finder is the primary discharge passage for the inner vortex in a hydrocyclone (Y. Zhang et al., 2023). In addition to conveying fine particles and most of the liquid phase out of the unit, it alters the geometric boundary of the inner-vortex passage and thereby affects internal flow partitioning and particle motion. Its diameter (Vieira et al., 2016), insertion depth (He et al., 2022), wall thickness (Zhao

DOI: 10.37190/ppmp/242520

et al., 2019; Wu et al., 2025), and structural configuration (Jiang et al., 2020) all modify the flow state of the inner vortex, which in turn influences short-circuit flow formation and particle partitioning between the overflow and underflow (Ghodrat et al., 2014). By determining the available discharge area, the vortex finder diameter influences the overflow capacity, split ratio, separation cut size, and separation efficiency; therefore, its selection should depend on whether the hydrocyclone is intended for classification or thickening (Hashe and Kunene, 2023). When the vortex finder is inserted too shallowly, particles that have not been fully separated can readily enter the overflow through short-circuit flow. Excessive insertion depth, however, occupies effective separation space, shortens the particle separation path, and disturbs the stable motion of the inner vortex and outer vortex (He et al., 2020). Consequently, changing either the vortex finder diameter or its insertion depth in isolation is generally unable to balance the requirements for overflow fineness, underflow yield, and classification efficiency.

On the basis of conventional dimensional optimization of the vortex finder, researchers have further developed non-conventional vortex finders with thick-walled configurations (Martínez et al., 2008; X. Li et al., 2025), conical configurations (Li et al., 2021a), arc-shaped configurations (Hwang and Chou, 2017), and slotted configurations (Li et al., 2021b; Chen et al., 2024). By modifying the local flow boundary near the overflow discharge opening and the configuration of the flow channel (F. Li et al., 2025), these designs regulate the internal velocity field (Liu et al., 2023), suppress short-circuit flow (T. Zhang et al., 2023), and improve particle partitioning (Vakamalla et al., 2017). Numerical and experimental reviews show that CFD, together with experimental validation, can relate cyclone geometry and operating parameters to swirling flow and separation performance (Dehdarinejad and Bayareh, 2021; Bayareh, 2024). In addition, variable-pitch spiral guide vanes have been shown to modify the flow field, particle collection, and erosion, demonstrating the value of internal flow-guiding structures for separator optimization (Dehdarinejad and Bayareh, 2022b). Although gas–solid cyclones differ from liquid–solid hydrocyclones, these studies support the general strategy of combining structural modification with numerical and experimental evaluation. Although these structures can improve classification or thickening performance under specific operating conditions, their geometric parameters are typically fixed after fabrication and installation and therefore cannot be adjusted dynamically to accommodate changes in feed concentration, feed pressure, or classification objectives. To overcome this limitation, we previously developed an overflow-adjustable hydrocyclone (Li et al., 2026), in which the effective overflow cross-sectional area was regulated by adjusting the baffle parameters. Previous work established the feasibility of the adjustable overflow structure and compared its classification behavior with that of a conventional hydrocyclone. However, that study focused primarily on structural feasibility and baffle diameter. The effects of feed concentration, feed pressure, and baffle height on OAHC classification performance, as well as parameter selection under different evaluation objectives, remain to be systematically clarified.

As hydrocyclone applications have expanded from particle-size classification to thickening, dewatering, and energy-efficient operation (Ji et al., 2023), parameter selection has increasingly shifted from single-metric evaluation to coordinated multi-criteria evaluation (Kyriakidis et al., 2018). Accordingly, recent research has increasingly employed multi-objective optimization together with preference-based decision frameworks, reliability-oriented design, and structural optimization to systematically evaluate the trade-offs among separation performance, classification accuracy, and energy-related objectives (Garcia et al., 2024; Tan et al., 2024; E et al., 2025). For example, Ullmann et al. evaluated the underflow-to-throughput ratio, separation efficiency, and energy consumption as concurrent objectives when optimizing thickening hydrocyclones (Ullmann et al., 2021). Toprak and Altun selected hydrocyclone operating conditions by considering underflow solids content, product particle-size distribution, and downstream paste-backfill requirements (Toprak and Altun, 2021). Orthogonal experiments and response surface methodology are commonly used to identify parameter effects and interactions (Tang et al., 2015). Grey relational analysis (GRA) provides a practical approach for combining multiple responses with different units into a single relational grade by evaluating their proximity to an ideal reference sequence (Liu et al., 2022). It is therefore suitable for comparing discrete orthogonal experimental Runs when improvement in one response may be accompanied by deterioration in another. However, GRA-based coordinated selection of adjustable overflow structures and operating parameters under different operating conditions has not been systematically investigated.

Building on our previous validation of the OAHC structure (Li et al., 2026), the present study examines the effects of feed concentration, feed pressure, and baffle height on classification performance and evaluates parameter selection under multiple objectives. An $L_9(3^3)$ orthogonal experiment was conducted using feed pressure, baffle diameter, and baffle height as the factors, with underflow yield, overflow fineness, and classification efficiency as the evaluation metrics. Weighted GRA and factor-level main-effect analysis were then used to identify a preferred multi-criteria combination, which was subsequently evaluated in a confirmation experiment.

2. Experimental study

2.1. Experimental system and equipment

An industrial-scale OAHC with a cylindrical-section diameter of 350 mm was used in the experiments. The OAHC contains a movable cylindrical baffle inside the conical overflow pipe. An actuator-driven screw moves the baffle axially: raising the baffle decreases the annular overflow passage and the effective overflow area, thereby increasing upward flow resistance, whereas lowering it produces the opposite effect. Fig. 1 illustrates the experimental circuit, geometric configuration of the OAHC, and physical test rig, while Table 1 summarizes the principal dimensions of the device.

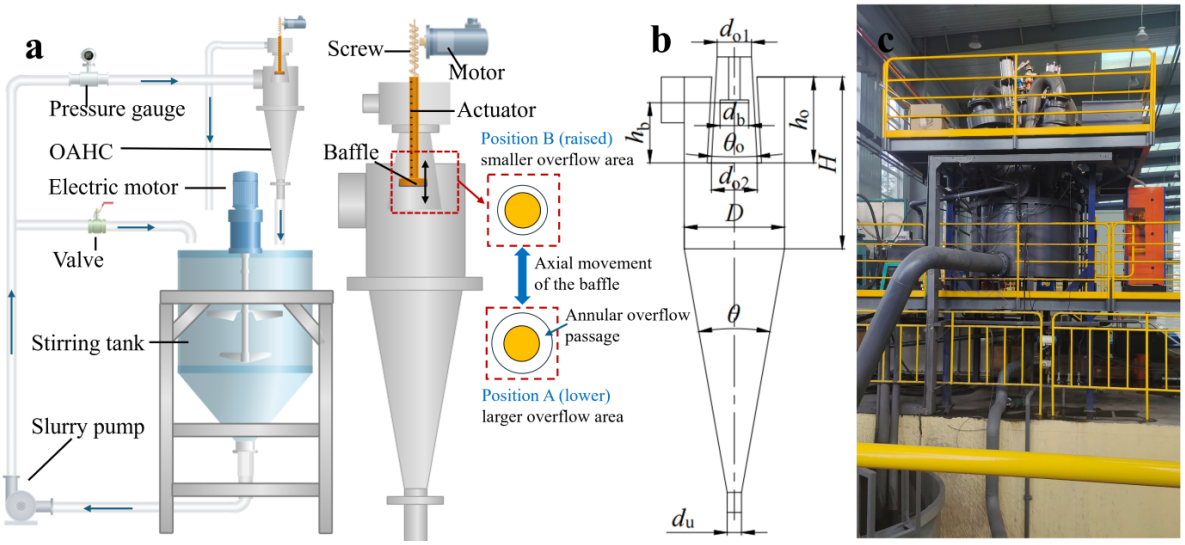


Fig. 1. Experimental apparatus and OAHC configuration: (A) layout of the experimental circuit; (B) dimensional schematic of the OAHC; and (C) photograph of the test rig

Table 1. Structural parameters of the OAHC used in the experiments.

Structural parameter	Size	Structural parameter	Size
Cylinder diameter (mm)	350	Conical angle θ_o (°)	6
Cylinder height H (mm)	600	Vortex finder diameter d_o (mm)	120
Cone angle θ (°)	20	Upper vortex finder diameter d_{o1} (mm)	120
Feed inlet dimensions (mm)	160×60	Lower vortex finder diameter d_{o2} (mm)	160
Underflow diameter d_u (mm)	50	Baffle diameter d_b (mm)	85, 100, 115
Vortex finder insertion depth h_o (mm)	300	Baffle height h_b (mm)	60, 110, 160, 210, 260, 310

Iron ore and water were used to prepare slurries with different solids concentrations. The slurry was homogenized in a stirred tank and fed to the OAHC by a centrifugal pump. The slurry was recirculated

through a closed-loop circuit to maintain feed uniformity. After the system had reached steady state for 10 min, samples were collected simultaneously from the feed, overflow, and underflow streams to ensure that they represented the same operating condition. All single-factor operating conditions, all nine factor combinations in the $L_9(3^3)$ orthogonal experiment, the additional A_1B_1 tests, and the $A_1B_3C_3$ confirmation experiment were independently tested three times. All response values are reported as means ± standard deviations (mean ± SD, n = 3), and the error bars represent one standard deviation.

2.2. Experimental material

The experimental feed was collected from an iron-ore grinding circuit and had a material density of 3400 kg/m³. Its particle-size distribution was determined by sieve analysis; the resulting differential and cumulative distributions are summarized in Table 2. Particles smaller and larger than 74 μm accounted for 52.06% and 47.94% of the feed, respectively. Because these two fractions occurred in comparable proportions, the −74 μm fraction was used as the reference fraction for calculating overflow fineness and classification efficiency.

Table 2. Differential and cumulative size distributions of the iron-ore feed.

Sieve No.	Particle-size interval (μm)	Representative size (μm)	Mass fraction (%)	Cumulative undersize (%)
60	>300	300	8.42	100
100	154−300	227	19.47	91.58
150	100−154	127	11.06	72.11
200	74−100	87	8.99	61.05
325	45−74	59.5	13.02	52.06
500	30−45	37.5	7.07	39.04
–	<30	15	31.97	31.97

2.3. Experimental design

The structural parameters of the OAHC are listed in Table 1, and the levels used in the single-factor experiments are presented in Table 3. During the feed-concentration tests, the feed pressure was maintained at 0.14 MPa, with the baffle diameter and height set at 100 and 160 mm, respectively. For the feed-pressure tests, the feed concentration was held at 38%, while the baffle diameter and height remained at 100 and 160 mm, respectively. In the baffle-height tests, the feed concentration and pressure were maintained at 49% and 0.14 MPa, respectively, and the baffle diameter was fixed at 100 mm.

Table 3. Experimental factors and levels.

Factors	Levels
Feed concentration (%)	28.5, 33.7, 38.1, 42.8, 46.8, 51.9
Feed pressure (MPa)	0.08, 0.10, 0.12, 0.14, 0.16, 0.18
Baffle height (mm)	60, 110, 160, 210, 260, 310

Based on the feed-concentration tests and the previous comparison between a conventional hydrocyclone and the OAHC, the feed concentration was fixed at 44% as a representative high-solids stress condition. This level was between the tested concentrations of 42.8% and 46.8%, at which overflow fineness and classification efficiency had begun to decline. An $L_9(3^3)$ orthogonal design was conducted with feed pressure (A), baffle diameter (B), and baffle height (C) as factors, and underflow yield, overflow fineness, and classification efficiency as responses. The pressure and height levels were selected from the response-sensitive ranges identified in the single-factor tests, while baffle diameters

of 85, 100, and 115 mm were selected from the feasible response-sensitive range established by the previous 55-130 mm study (Li et al., 2026), with 100 mm as the reference level. These diameters were treated as bounded structural factors rather than as a repeat of the previous standalone study. Additional A_1B_1 tests examined the C_2 baffle-height level, followed by an $A_1B_3C_3$ confirmation experiment at a feed concentration of 44%, a feed pressure of 0.12 MPa, a baffle diameter of 115 mm, and a baffle height of 260 mm. Weighted GRA ranked the nine orthogonal runs, whereas main-effect analysis predicted the factor-level combination for confirmation. Because the confirmation condition produced a higher classification efficiency than the original runs, all ten conditions were normalized using common fixed ranges and GRA parameters, and ranking stability was assessed using Spearman's rank correlation coefficient.

2.4. Classification performance indices

The classification performance of the OAHC was evaluated using underflow yield, split ratio, the Tromp curve and cut size, classification efficiency, and cumulative undersize distribution.

2.4.1. Underflow yield

The underflow yield represents the percentage of the solids entering with the feed that is recovered in the underflow and is calculated as follows:

$$E_t = \frac{M_u C_u}{M_i C_i} \times 100\% \tag{1}$$

where E_t is the underflow yield, %; M_i and M_u denote the slurry mass flow rates of the feed and underflow streams, respectively, in t/h; and C_i and C_u represent their corresponding solids mass concentrations, %.

2.4.2. Split ratio

The split ratio represents the fraction of the feed volumetric flow discharged through the underflow and is expressed as:

$$S_u = Q_u/Q_i \tag{2}$$

where S_u is the split ratio, and Q_u and Q_i represent the volumetric flow rates of the underflow and feed streams, respectively, in m^3/h.

2.4.3. Tromp curve and cut size

The Tromp curve describes the relationship between particle size and the proportion of each feed size fraction recovered in the underflow. The corresponding partition number is calculated as follows:

$$G(d_s) = E_t \frac{f_u(d_s)}{f_i(d_s)} \tag{3}$$

where $G(d_s)$ is the partition number for particles of size d_s, %; E_t is the underflow yield, %; $f_i(d_s)$ and $f_u(d_s)$ represent the mass fractions of size d_s in the feed and underflow streams, respectively, %; and d_s is the particle size, μm.

The cut size, denoted by d_{50}, is the particle diameter at which the partition number reaches 50%. Particles of this size therefore have equal probabilities of entering the underflow and overflow.

2.4.4. Classification efficiency

The classification efficiency was used to characterize the separation of the specified size fraction and the extent of coarse–fine particle mixing in the products. It was calculated as follows:

$$E_c = \frac{(\alpha-\gamma)(\beta-\alpha)}{\alpha(\beta-\gamma)(100-\alpha)} \times 10000\% \tag{4}$$

where E_C is the classification efficiency, %; and a, β, and γ represent the percentages of the specified size fraction in the feed, overflow, and underflow streams, respectively.

2.4.5. Cumulative undersize distribution

The cumulative undersize distribution quantifies the mass proportion of particles not exceeding a specified size and is determined as follows:

$$Q(d_k) = \frac{\sum_{i=1}^{k} m_i}{M} \times 100\% \quad (5)$$

where $Q(d_k)$ is the cumulative undersize distribution at particle size d_k, %; k is the number of size fractions with particle sizes less than or equal to d_k; m_i is the mass of the i-th size fraction, kg; and M is the total sample mass, kg.

3. Results and discussion

3.1. Single-factor experiments

3.1.1. Effect of feed concentration on OAHC classification performance

Fig. 2 shows that increasing the feed concentration from 28.5% to 51.9% reduced the underflow yield from 62.18% to 44.25%, whereas the split ratio increased from 0.1313 to 0.1760. Over the same range, the underflow concentration increased from 77.29% to 84.25%, while the overflow concentration increased from 13.96% to 39.83%, indicating a stronger effect on the overflow. Previous CFD and high-solids studies have shown that increasing solids concentration modifies turbulence and strengthens particle interactions, thereby altering radial particle migration and increasing coarse-particle misplacement to the overflow (Kuang et al., 2012; Kumar et al., 2021; Padhi et al., 2021). The present results are consistent with this mechanism.

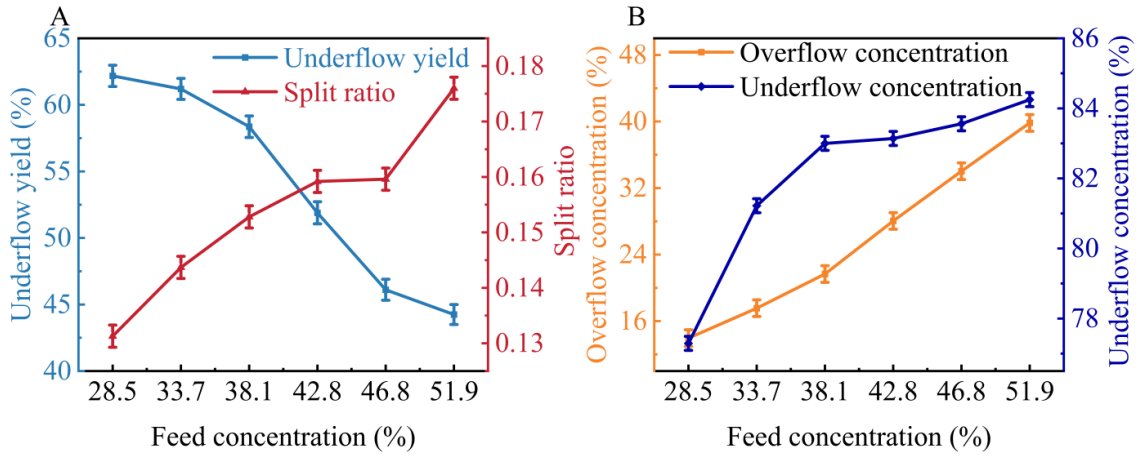


Fig. 2. Responses of (A) underflow yield and split ratio and (B) product concentrations to feed concentration

Fig. 3 shows that the cumulative undersize curves for both products shifted toward coarser particle sizes as feed concentration increased. The −74 μm fraction in the overflow decreased from 95.61% to 77.27%, while that in the underflow decreased from 27.89% to 21.24%. At higher concentrations, increased solids loading, slurry viscosity, and particle interference may have hindered the outward migration and prompt discharge of some coarse particles, allowing them to migrate inward and subsequently leave through the overflow. Together with the size-distribution results, the pronounced increase in overflow concentration indicated that more solids, including coarse material, entered the overflow stream.

The cut size rose from 53.65 μm to 84.06 μm as the feed concentration increased, whereas the partition numbers declined across all size fractions (Fig. 4). Classification efficiency decreased from 63.56% to 55.21%. Higher slurry viscosity and more frequent particle–particle collisions may have weakened effective centrifugal separation. Some coarse particles may not have been discharged promptly through the underflow outlet and may instead have migrated inward into the inner vortex before leaving through the overflow.

Overall, increasing feed concentration likely increased slurry viscosity and intensified particle–particle interactions, thereby restricting particle motion and weakening effective centrifugal separation

for both coarse and fine particles. Because the underflow outlet had limited discharge capacity, some coarse particles may not have been discharged promptly and may instead have migrated toward the inner vortex before reporting to the overflow, resulting in overflow coarsening and an increased cut size. Although fine-particle misplacement to the underflow decreased, this benefit was insufficient to offset the deterioration in overflow fineness, and classification efficiency therefore declined. Consequently, a single operating parameter could not maintain overflow fineness, underflow yield, and classification efficiency simultaneously as feed concentration increased. The combined effects of feed pressure, baffle diameter, and baffle height were therefore investigated in the orthogonal experiments.

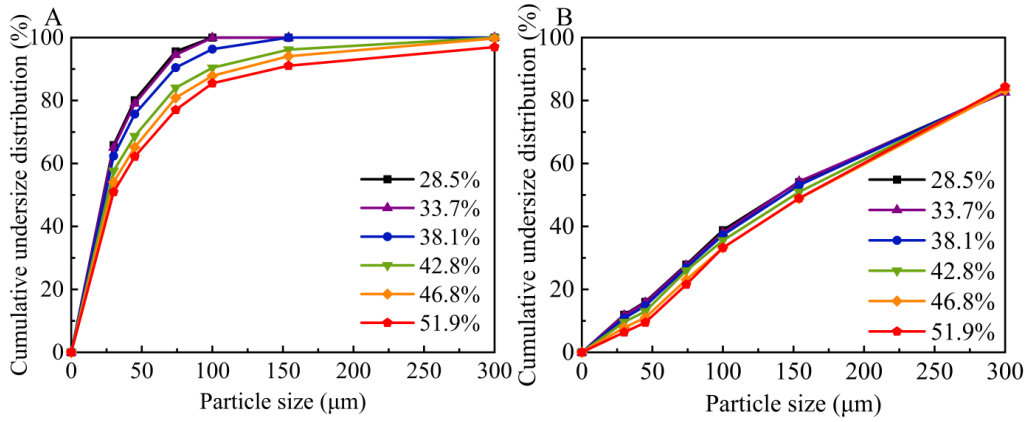


Fig. 3. Cumulative undersize distributions of (A) overflow and (B) underflow products at different feed concentrations

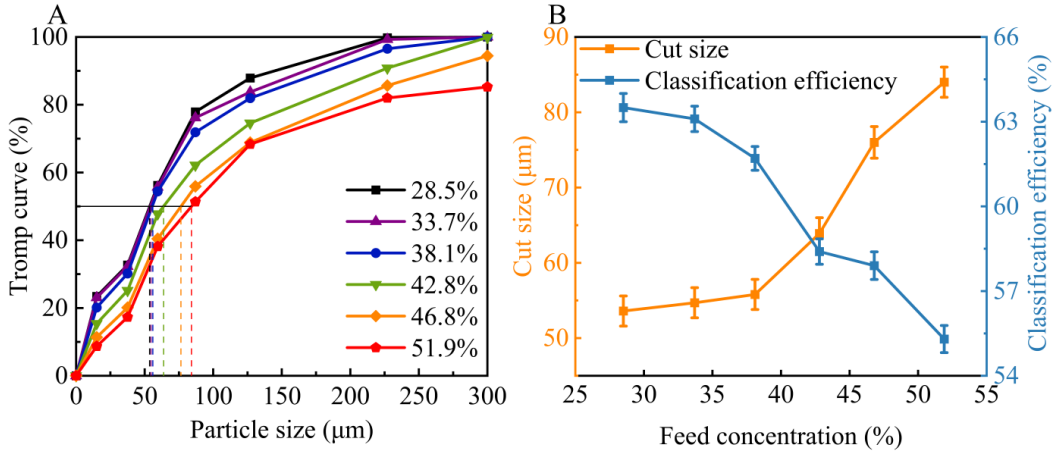


Fig. 4. (A) Tromp curves and (B) d_{50} and classification efficiency at different feed concentrations.

3.1.2. Effect of feed pressure on OAHC classification performance

Fig. 5 shows that when the feed pressure rose from 0.08 MPa to 0.18 MPa, the underflow yield increased from 56.41% to 60.06%, while the underflow concentration increased from 76.82% to 81.29%. In contrast, the split ratio fell from 0.1780 to 0.1676, whereas the overflow concentration decreased from 23.26% to 21.46%. An increase in feed pressure increased the inlet flow rate and strengthened the internal swirling motion. Meanwhile, the associated change in water distribution between the overflow and underflow also affected the separation performance. As the proportion of slurry volume discharged through the underflow declined, the split ratio decreased accordingly.

Fig. 6 shows that the cumulative undersize curves of the overflow and underflow products shifted toward smaller particle sizes as feed pressure increased. When the pressure rose from 0.08 MPa to 0.18 MPa, the −74 μm fraction in the overflow increased from 85.40% to 87.97%, corresponding to an improvement of 2.57 percentage points in overflow fineness. Over the same pressure range, the −74 μm fraction in the underflow increased from 26.40% to 28.74%. This increase of 2.34 percentage points indicates greater fine-particle misplacement to the underflow.

This response may be related to the stronger outward migration of particles at higher feed pressures, which made coarse particles less likely to enter the overflow. However, the enhanced centrifugal action and disturbance of the flow field may also have diverted some fine particles from the inner vortex toward the outer vortex, causing them to be discharged through the underflow. Thus, increasing the feed pressure improved overflow fineness but also aggravated the misplacement of fine particles to the underflow.

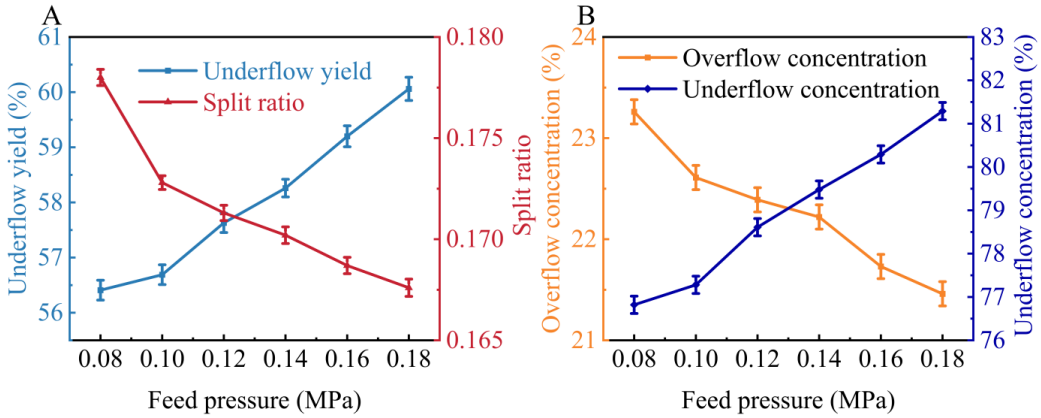


Fig. 5. Responses of (A) underflow yield and split ratio and (B) product concentrations to feed pressure

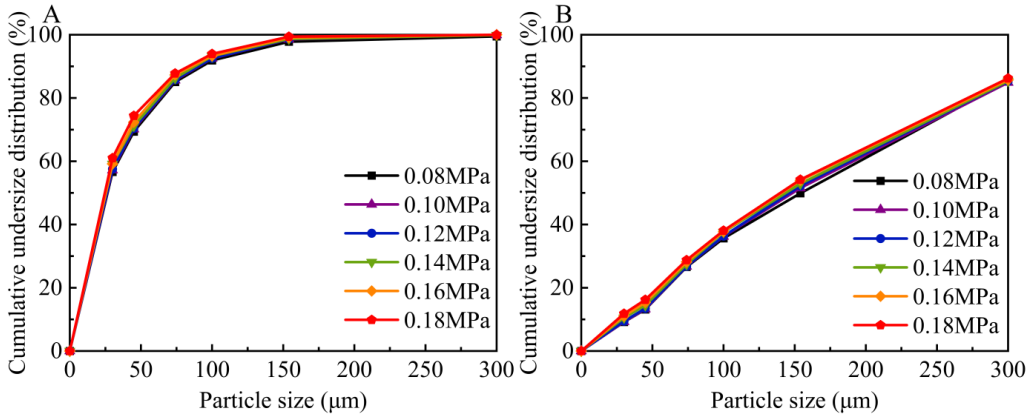


Fig. 6. Cumulative undersize distributions of (A) overflow and (B) underflow products at different feed pressures

Fig. 7 shows that the cut size decreased from 59.88 μm to 51.42 μm as the feed pressure increased. Although higher feed pressure improved overflow fineness and underflow yield, it also intensified fine-particle misplacement to the underflow. Consequently, classification efficiency decreased from 58.93% to 56.68%.

Overall, increasing the feed pressure increased the inlet flow rate and strengthened the centrifugal field, while the accompanying change in water distribution further influenced the separation performance within the OAHC. The stronger centrifugal action drove coarse particles outward toward the outer vortex, thereby increasing the underflow yield, decreasing the cut size, and improving overflow fineness. However, at excessively high feed pressures, some fine particles could also overcome the inward fluid drag and enter the outer vortex before leaving through the underflow outlet. Consequently, the gain in overflow fineness was insufficient to offset the greater fine-particle misplacement to the underflow, which led to a decline in classification efficiency. Moreover, a higher feed pressure may increase the energy demand of the system. Therefore, feed pressure should be selected by jointly considering overflow fineness, underflow yield, and classification efficiency.

3.1.3. Effect of baffle height on OAHC classification performance

Fig. 8 shows that increasing the baffle height from 60 mm to 310 mm raised the underflow yield

from49.84% to 63.66% and the split ratio from 0.1961 to 0.3497. Meanwhile, the underflow concentration declined from 82.22% to 70.48%, whereas the overflow concentration fell from 35.67% to 32.87%. Increasing baffle height reduced the effective overflow cross-sectional area and increased flow resistance, redirecting a larger volumetric fraction of slurry to the underflow. Because the increase in volumetric flow to the underflow was relatively large, the underflow slurry was diluted.

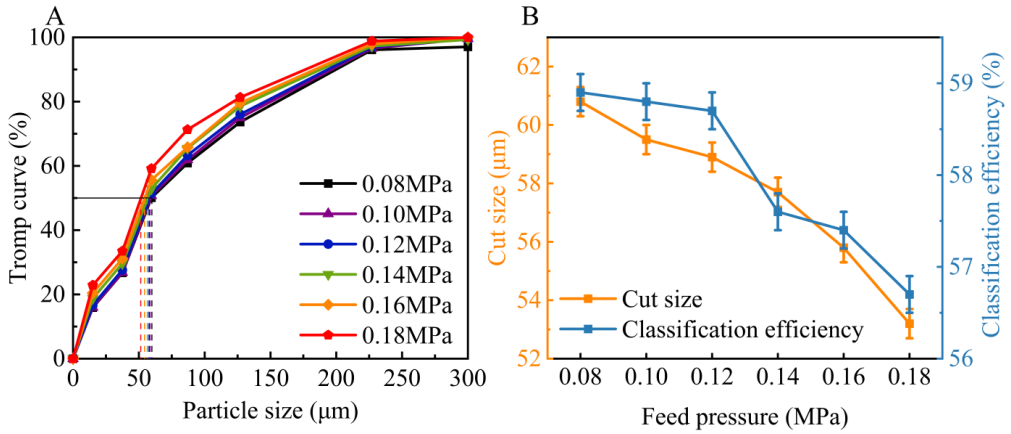


Fig. 7. (A) Tromp curves and (B) d_{50} and classification efficiency at different feed pressures

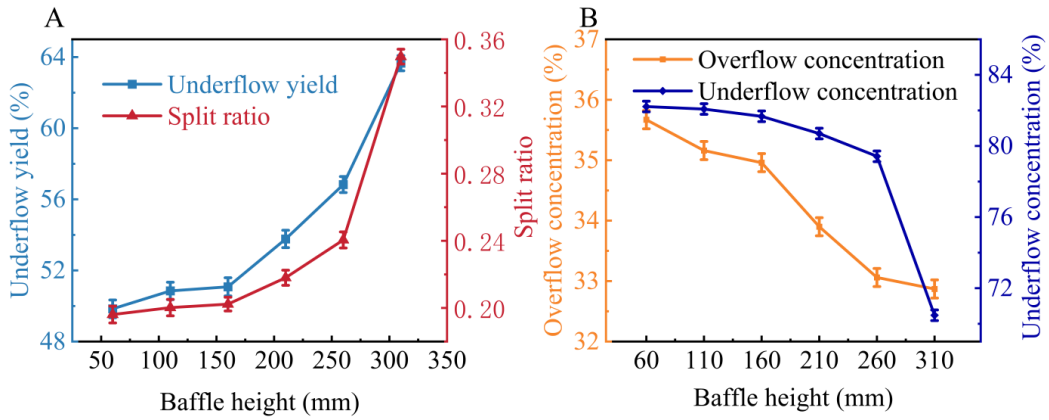


Fig. 8. Responses of (A) underflow yield and split ratio and (B) product concentrations to baffle height

Fig. 9 indicates that the cumulative undersize curves of both product streams shifted toward smaller particle sizes as the baffle height increased. The −74 μm fraction increased from 77.79% to 86.40% in the overflow and from 23.16% to 30.15% in the underflow. A more restricted overflow passage reduced the carryover of coarse particles into the overflow but increased fine-particle misplacement to the underflow. Some fine particles may have entered the outer vortex and subsequently left through the underflow outlet. Thus, increasing the baffle height produced a trade-off: overflow fineness improved, whereas the loss of fine particles to the underflow increased.

Fig. 10 shows that the Tromp curves moved toward smaller particle sizes as the baffle height increased. Meanwhile, the cut size fell from 71.75 μm to 49.85 μm, indicating that fine particles became more likely to enter the underflow. Classification efficiency rose initially but declined thereafter, reaching its highest value of 56.34% at a baffle height of 210 mm.

Our previous CFD study of the OAHC showed that the built-in baffle strengthened tangential motion in the main separation region and reduced the upward axial motion of the inner vortex. This effect prolonged particle residence time and reduced the likelihood of coarse particles entering the overflow (Li et al., 2026). In the present OAHC, a moderate baffle height therefore likely limited coarse-particle transfer into the overflow, whereas excessive baffle height may have excessively restricted the upward inner-vortex flow and redirected some fine particles toward the outer vortex and underflow.

With feed concentration fixed at 44% following the single-factor evaluation, the combined effects of feed pressure, baffle diameter, and baffle height were subsequently investigated using the orthogonal design.

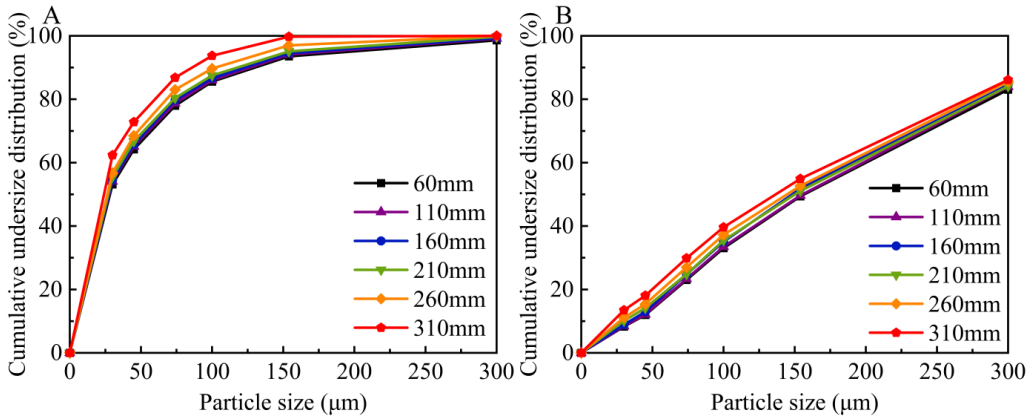


Fig. 9. Cumulative undersize distributions of (A) overflow and (B) underflow products at different baffle heights

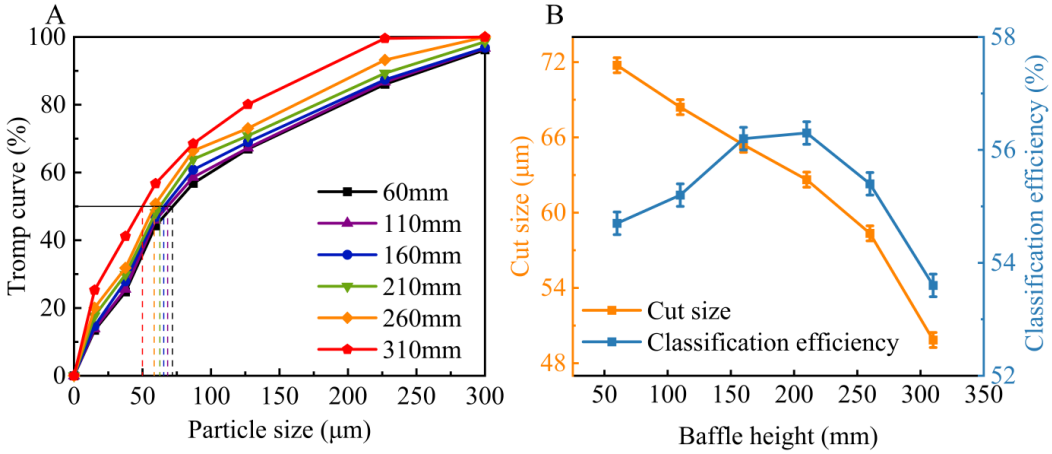


Fig. 10. (A) Tromp curves and (B) d_{50} and classification efficiency at different baffle heights

3.2. Orthogonal experiment

Table 4 lists the three levels assigned to feed pressure (factor A), baffle diameter (factor B), and baffle height (factor C). An $L_9(3^3)$ orthogonal array was used to evaluate the effects of these factors on underflow yield, overflow fineness, and classification efficiency. Each factor combination was tested independently in triplicate. Table 5 reports the response values as mean ± SD (n = 3). These replicates provided an estimate of within-condition experimental variability, and the mean response at each condition was used for the subsequent range analysis and weighted GRA. However, because the L_9 orthogonal array was designed primarily for main-effect screening, it did not allow all factor interactions to be resolved independently. Accordingly, the factor rankings and preferred combinations were interpreted within the investigated factor levels.

Table 4. Factors and levels used in the orthogonal experiment

Level	Feed pressure (MPa)	Baffle diameter (mm)	Baffle height (mm)
1	0.12	85	160
2	0.14	100	210
3	0.16	115	260

3.2.1. Parameter selection based on underflow yield

As shown in Table 6, range analysis predicted $A_3B_3C_3$ as the preferred combination for underflow yield within the investigated levels, corresponding to a feed pressure of 0.16 MPa, a baffle diameter of 115

mm, and a baffle height of 260 mm. The range-based factor ordering was baffle diameter > baffle height > feed pressure, with baffle diameter exhibiting the largest range (R = 4.25). Increasing the baffle diameter and height reduced the effective overflow cross-sectional area and caused more solids to report to the underflow. However, a higher underflow yield alone does not indicate superior overall classification performance.

Table 5. Results of the $L_9(3^3)$ orthogonal experiment expressed as mean ± SD (n = 3)

Run No.	A: Feed pressure (MPa)	B: Baffle diameter (mm)	C: Baffle height (mm)	Underflow yield (%)	Overflow fineness (%)	Classification efficiency (%)
1	0.12	85	160	51.55 ± 0.31	86.25 ± 0.25	60.48 ± 0.20
2	0.12	100	260	52.74 ± 0.29	85.88 ± 0.24	59.53 ± 0.18
3	0.12	115	210	57.46 ± 0.30	86.98 ± 0.26	58.85 ± 0.21
4	0.14	85	260	54.68 ± 0.29	86.44 ± 0.22	58.49 ± 0.19
5	0.14	100	210	54.28 ± 0.28	86.52 ± 0.25	59.53 ± 0.22
6	0.14	115	160	53.36 ± 0.32	85.01 ± 0.26	57.67 ± 0.19
7	0.16	85	210	55.86 ± 0.34	86.69 ± 0.20	58.49 ± 0.20
8	0.16	100	160	53.25 ± 0.27	84.73 ± 0.20	57.73 ± 0.21
9	0.16	115	260	62.21 ± 0.26	89.75 ± 0.20	58.18 ± 0.25

Table 6. Factor-level mean responses, range analysis, and selected levels for the three separation performance indices

Evaluation metric	Statistic	A: Feed pressure (MPa)	B: Baffle diameter (mm)	C: Baffle height (mm)
Underflow yield	k_{1j}	53.92	54.03	52.72
	k_{2i}	54.11	53.42	55.87
	k_{3j}	57.11	57.68	56.54
	Selected factor level	A_3	B_3	C_3
	R	3.19	4.25	3.82
Overflow fineness	k_{1j}	86.37	86.46	85.33
	k_{2i}	85.99	85.71	86.73
	k_{3i}	87.06	87.25	87.36
	Selected factor level	A_3	B_3	C_3
	R	1.07	1.54	2.03
Classification efficiency	k_{1j}	59.62	59.15	58.63
	k_{2i}	58.56	58.93	58.96
	k_{3j}	58.13	58.23	58.73
	Selected factor level	A_1	B_1	C_2
	R	1.49	0.92	0.33

3.2.2. Parameter selection based on overflow fineness

For overflow fineness, range analysis also predicted $A_3B_3C_3$ as the preferred combination within the investigated levels. The range-based factor ordering was baffle height > baffle diameter > feed pressure, with baffle height exhibiting the largest range (R = 2.03). Increasing the baffle height reduced the available flow area of the overflow passage, making coarse particles less likely to leave through the overflow. However, larger baffle heights and diameters may also promote the misplacement of fine particles to the underflow; classification efficiency must therefore be considered during parameter selection.

3.2.3. Parameter selection based on classification efficiency

When classification efficiency was used as the evaluation metric, range analysis predicted $A_1B_1C_2$ as the preferred combination within the investigated levels, corresponding to a feed pressure of 0.12 MPa, a baffle diameter of 85 mm, and a baffle height of 210 mm. The range-based factor ordering was feed pressure > baffle diameter > baffle height, with feed pressure exhibiting the largest range (R = 1.49). Although higher feed pressure, a larger baffle diameter, and a greater baffle height generally improved underflow yield and overflow fineness, they may also have increased fine-particle misplacement to the underflow. Therefore, $A_1B_1C_2$ was preferred when classification efficiency was considered as the sole evaluation objective.

3.2.4. Additional experiments under the A_1B_1 condition

Additional experiments were conducted under the A_1B_1 condition to examine whether the C_2 level predicted by range analysis provided a higher classification efficiency than the adjacent C_1 and C_3 levels. Feed concentration, feed pressure, baffle diameter, and underflow outlet diameter were fixed at 44%, 0.12 MPa, 85 mm, and 50 mm, respectively. Baffle heights of 160, 210, and 260 mm were tested using the same steady-state sampling and measurement procedures described in Section 2.1.

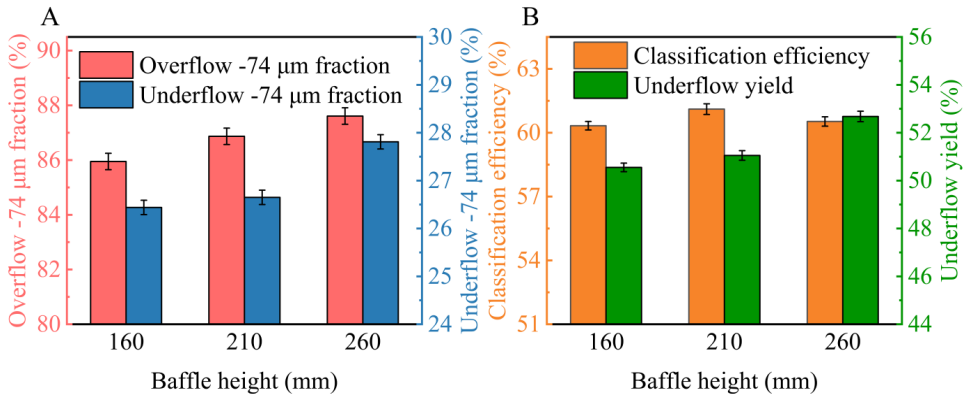


Fig. 11. Additional experimental results under the A_1B_1: (A) -74 μm contents; (B) classification efficiency and underflow yield

As shown in Fig. 11, at a feed pressure of 0.12 MPa and a baffle diameter of 85 mm, overflow fineness increased with baffle height, whereas classification efficiency first increased and then decreased. At a baffle height of 210 mm, classification efficiency and overflow fineness reached 61.11% and 86.87%, respectively. Among the three baffle heights examined under the A_1B_1 condition, C_2 produced the highest observed classification efficiency. These additional experiments therefore provided local support for selecting C_2 when classification efficiency was prioritized under A_1B_1. They were not intended to validate the overall multi-criteria ranking and were not included in the subsequent GRA, which was based exclusively on the original nine orthogonal runs.

3.2.5. Multi-criteria evaluation based on weighted grey relational analysis

As shown in Table 7, the preferred factor-level combinations differed among the three individual evaluation metrics, indicating a trade-off among underflow yield, overflow fineness, and classification

efficiency. Weighted GRA was therefore used to integrate the three larger-the-better responses into a single grey relational grade. The normalized responses and grey relational coefficients are shown in Fig. 12. Run 9 exhibited the highest underflow yield and overflow fineness, whereas Run 1 exhibited the highest classification efficiency, further demonstrating the conflicting tendencies among the three responses. The calculation equations, weight-sensitivity results, expanded grey relational grades, and ranking stability are provided in the Supporting Information (Eqs. (S1)–(S4), Fig. S1, and Table S1).

Table 7. Factor-level combinations predicted by range analysis for the three individual evaluation metrics

Evaluation metric	Range-analysis prediction	Order of factor influence
Underflow yield	$A_3B_3C_3$	B > C > A
Overflow fineness	$A_3B_3C_3$	C > B > A
Classification efficiency	$A_1B_1C_2$	A > B > C

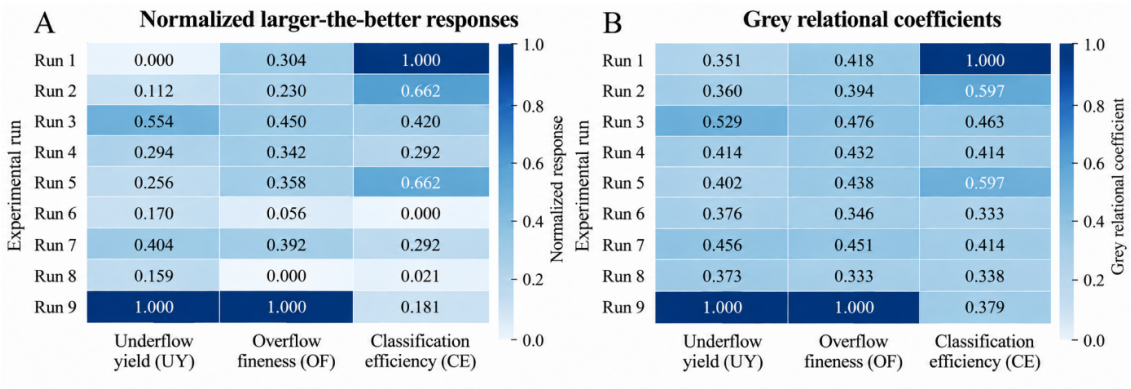


Fig. 12. Grey relational analysis matrices: (A) normalized responses; (B) grey relational coefficients

Based on industrial production requirements, the baseline weight allocation was set as 0.30, 0.30, and 0.40 for underflow yield, overflow fineness, and classification efficiency, respectively. The grey relational grades decreased in the order Run 9 > Run 1 > Run 5 > Run 3 > Run 2 > Run 7 > Run 4 > Run 6 > Run 8, as shown in Fig. 13. Run 9 achieved the highest grey relational grade of 0.7517, followed by Run 1 with a grade of 0.6253. Run 9 ($A_3B_3C_3$), corresponding to a feed pressure of 0.16 MPa, a baffle diameter of 115 mm, and a baffle height of 260 mm, produced an underflow yield of 62.21%, an overflow fineness of 89.75%, and a classification efficiency of 58.18%. It was therefore identified as the best-performing Run within the original orthogonal array under the specified weights. The full three-weight sensitivity analysis showed that Run 9 ranked first in 171 of the 231 weight combinations (74.0%), whereas Run 1 ranked first in the remaining 60 combinations (26.0%). Run 9 was favored when greater importance was assigned to underflow yield or overflow fineness, while Run 1 was favored when classification efficiency dominated. No other original run became the highest-ranked option (see Supporting Information, Fig. S1).

Direct GRA ranked Run 9 highest among the nine experimentally tested runs, whereas main-effect analysis predicted $A_1B_3C_3$ as the preferred factor-level combination. Based on three independent replicates, Run 9 produced an underflow yield of 62.21 ± 0.26%, an overflow fineness of 89.75 ± 0.20%, and a classification efficiency of 58.18 ± 0.25%, whereas the corresponding values for $A_1B_3C_3$ were 58.62 ± 0.27%, 88.91 ± 0.19%, and 61.05 ± 0.29%, respectively. Thus, $A_1B_3C_3$ yielded a lower underflow yield and slightly lower overflow fineness but a higher classification efficiency than Run 9. After normalization using the common fixed validation scale, $A_1B_3C_3$ achieved a higher grey relational grade than Run 9 (0.8040 vs. 0.7482). The ranking of the original runs remained highly stable after renormalization, with a Spearman rank correlation coefficient of 0.983 (see Supporting Information, Table S1). Therefore, $A_1B_3C_3$ was identified as the preferred multi-response condition under the specified weights; this does not imply that it outperformed Run 9 for every individual response.

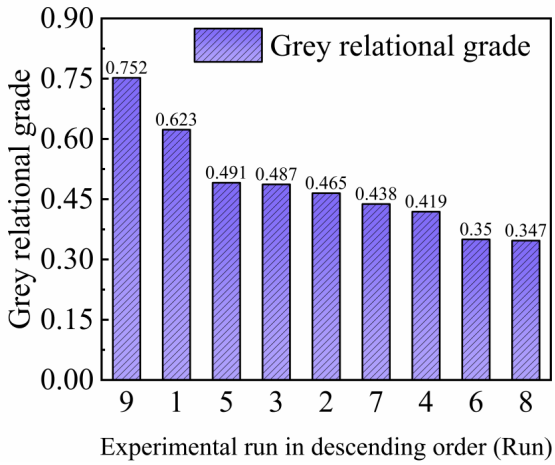


Fig. 13. Grey relational grades and ranking of the nine orthogonal experimental runs

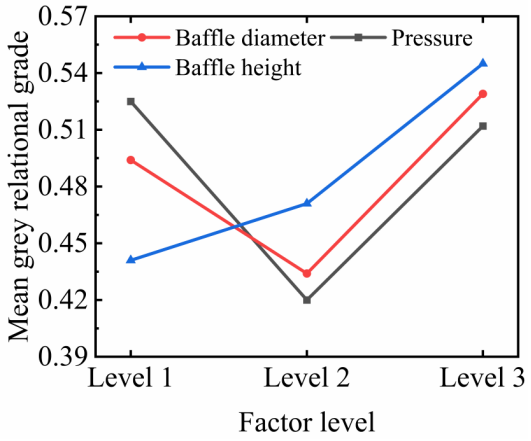


Fig. 14. Main effects of factor levels on the mean grey relational grade

3.3. Engineering considerations for industrial application

The OAHC used in this study had a cylindrical-section diameter of 350 mm, corresponding to an industrial-scale unit. In mineral-processing plants, treatment capacity would normally be increased by operating multiple hydrocyclones in parallel rather than by enlarging a single unit. Under these conditions, the performance of the adjustable baffle would depend not only on the operating parameters of each OAHC but also on uniform slurry distribution among the parallel units. Appropriate manifold design, branch-pressure monitoring, and flow regulation would therefore be needed to maintain comparable inlet pressure, solids concentration, and throughput across the units. Individual isolation valves would allow a unit to be inspected or serviced without shutting down the entire cluster.

The main energy penalty of the adjustable baffle is expected to result from the additional hydraulic resistance created when it restricts the effective overflow area. This may increase the required pressure drop and slurry-pumping power, while the parallel manifold may introduce additional distribution losses. The actuator operates only during adjustment; however, neither the additional pressure loss nor the actuator power was quantified in the present study. Future industrial trials should therefore evaluate pressure drop, throughput, and specific energy consumption at both the individual-unit and cluster levels.

Surface condition should also be considered because wear-induced roughness may affect both durability and separation performance. CFD results for gas–solid cyclones show that non-uniform wall roughness alters the flow pattern, pressure drop, collection efficiency, and erosion rate (Dehdarinejad and Bayareh, 2022a). Although the present OAHC treats a liquid–solid slurry, this finding highlights the need to consider wear as both a maintenance and performance issue. For abrasive iron-ore slurries, replaceable wear-resistant inserts or liners should therefore be provided at the baffle edge, overflow

passage, guide components, and slurry-side seals, together with protected transmission and sealing components and convenient external access.

4. Conclusions

This study investigated the classification performance and multi-criteria optimization of the previously developed overflow-adjustable hydrocyclone (OAHC) under varying operating conditions.

1. Feed concentration, feed pressure, and baffle height all affected OAHC classification performance. As feed concentration increased from 28.5% to 51.9%, overflow fineness decreased from 95.61% to 77.27%, while classification efficiency declined from 63.56% to 55.21%. Raising the feed pressure from 0.08 MPa to 0.18 MPa increased the underflow yield and overflow fineness; however, it also caused greater misplacement of fine particles to the underflow, resulting in a decline in classification efficiency from 58.93% to 56.68%. As the baffle height increased, the overflow became finer and the cut size declined, whereas classification efficiency showed a non-monotonic response and peaked at 56.34% for a baffle height of 210 mm.
2. Within the investigated factor levels, the preferred factor-level combination depended on the individual evaluation metric. The preferred combination was $A_3B_3C_3$ when either underflow yield or overflow fineness was prioritized, whereas $A_1B_1C_2$ was preferred when classification efficiency was prioritized. Under the A_1B_1 condition, classification efficiency was highest at C_2 among the three evaluated baffle heights. This setting yielded overflow fineness and classification efficiency values of 86.87% and 61.11%, respectively.
3. Among the original orthogonal runs, Run 9 ($A_3B_3C_3$) achieved the highest grey relational grade of 0.7517 under the baseline weights of 0.30, 0.30, and 0.40 for underflow yield, overflow fineness, and classification efficiency, respectively. Main-effect analysis of the factor-level mean grades predicted $A_1B_3C_3$ as the preferred multi-criteria combination. The $A_1B_3C_3$ confirmation experiment produced an underflow yield of 58.62%, an overflow fineness of 88.91%, and a classification efficiency of 61.05%. After the confirmation condition and the original nine runs were combined and re-normalized, $A_1B_3C_3$ achieved the highest grey relational grade of 0.8040. Thus, the confirmation result was consistent with the main-effect prediction, and $A_1B_3C_3$ was identified as the preferred multi-response condition under the specified weights; it was not superior to Run 9 for every individual response. Because the experiments compared separate steady-state conditions rather than transient feed changes, the results provide a basis for selecting OAHC operating and baffle parameters after feed conditions change but do not establish real-time dynamic control performance. Future work should evaluate transient response and control lag during continuous feed fluctuations, together with flow distribution, pressure balance, specific energy consumption, and abrasive-wear durability when multiple 350 mm OAHCs are operated in parallel under industrial conditions.

Acknowledgments

This work was supported by National Natural Science Foundation of China (No. 22408213), National Key Research and Development Program of China (No. 2023YFC2907702), and Shandong Province Key Research and Development Program (No. 2026QYTSGC01025, 2024TSGC0658).

References

BAYAREH, M., 2024. *A Review of the Experimental Analysis of Gas–Solid Cyclone Separators.* ChemBioEng Rev. 11. https://doi.org/10.1002/cben.202400036

CHEN, S., LI, D., LI, J., ZHONG, L., 2024. *Optimization design of hydrocyclone with overflow slit structure based on experimental investigation and numerical simulation analysis.* Sci. Rep. 14, 1–21. https://doi.org/10.1038/s41598-024-68954-y

DEHDARINEJAD, E., BAYAREH, M., 2022a. *Impact of non-uniform surface roughness on the erosion rate and performance of a cyclone separator.* Chem. Eng. Sci. 249, 117351. https://doi.org/10.1016/j.ces.2021.117351

DEHDARINEJAD, E., BAYAREH, M., 2022b. *Performance improvement of a cyclone separator using spiral guide vanes with variable pitch length.* J. Brazilian Soc. Mech. Sci. Eng. 44, 516. https://doi.org/10.1007/s40430-022-03788-1

DEHDARINEJAD, E., BAYAREH, M., 2021. *An Overview of Numerical Simulations on Gas-Solid Cyclone Separators*

with Tangential Inlet. ChemBioEng Rev. 8, 375–391. https://doi.org/10.1002/cben.202000034

E, D., HU, H., YE, Q., TAN, C., CUI, J., ZHOU, Z., ZOU, R., YU, A., KUANG, S., 2025. *Multi-objective optimization of hydrocyclones inlet configurations for improving separation performance*. Powder Technol. 456, 120772. https://doi.org/10.1016/j.powtec.2025.120772

ENDRES, E., DUECK, J., NEESSE, T., 2012. *Hydrocyclone classification of particles in the micron range*. Miner. Eng. 31, 42–45. https://doi.org/10.1016/j.mineng.2011.10.013

GARCIA, V.A., NETO, R.M.F., LOBATO, F.S., VIEIRA, L.G.M., 2024. *Reliability-based design of high-performance hydrocyclones: Multi-objective optimization, fabrication using 3D-printing and experimental analysis*. Powder Technol. 435, 119427. https://doi.org/10.1016/j.powtec.2024.119427

GHODRAT, M., KUANG, S.B., YU, A.B., VINCE, A., BARNETT, G.D., BARNETT, P.J., 2014. *Numerical analysis of hydrocyclones with different vortex finder configurations*. Miner. Eng. 63, 125–138. https://doi.org/10.1016/j.mineng.2014.02.003

GIGLIA, K.C., ALDRICH, C., 2020. *Operational state detection in hydrocyclones with convolutional neural networks and transfer learning*. Miner. Eng. 149, 106211. https://doi.org/10.1016/j.mineng.2020.106211

HASHE, V.T., KUNENE, T.J., 2023. *Numerical Analysis of the Effect of the Vortex Finder on the Hydrocyclone's Split Water Ratio and Separation Performance*. Math. Comput. Appl. 28, 50. https://doi.org/10.3390/mca28020050

HE, F., WANG, H., WANG, J., LI, S., FAN, Y., XU, X., 2020. *Experimental study of mini-hydrocyclones with different vortex finder depths using Particle Imaging Velocimetry*. Sep. Purif. Technol. 236, 116296. https://doi.org/10.1016/j.seppur.2019.116296

HE, F., ZHAO, D., WANG, J., HUANG, Y., LIU, Q., 2022. *Numerical Simulation Investigation of Vortex Finder Depth Effects on Flow Field and Performance of Desanding Mini-Hydrocyclones*. J. Mar. Sci. Eng. 10. https://doi.org/10.3390/jmse10111600

HWANG, K.-J., CHOU, S.-P., 2017. *Designing vortex finder structure for improving the particle separation efficiency of a hydrocyclone*. Sep. Purif. Technol. 172, 76–84. https://doi.org/10.1016/j.seppur.2016.08.005

JI, L., PAUL, P., SHANBHAG, B.K., DIXON, I., KUANG, S., HE, L., 2023. *Emerging application of hydrocyclone in biotechnology and food processing*. *Sep. Purif. Technol.* 309, 122992. https://doi.org/10.1016/j.seppur.2022.122992

JIANG, L., LIU, P., YANG, X., ZHANG, Y., LI, X., ZHANG, Y., WANG, H., 2020. *Effect of Overflow Pipe on the Internal Flow Fields and Separation Performance of W-Shaped Hydrocyclones*. Minerals 10, 329. https://doi.org/10.3390/min10040329

KUANG, S.B., CHU, K.W., YU, A.B., VINCE, A., 2012. *Numerical study of liquid–gas–solid flow in classifying hydrocyclones: Effect of feed solids concentration*. Miner. Eng. 31, 17–31. https://doi.org/10.1016/j.mineng.2012.01.003

KUMAR, M., REDDY, R., BANERJEE, R., MANGADODDY, N., 2021. *Effect of particle concentration on turbulent modulation inside hydrocyclone using coupled MPPIC-VOF method*. Sep. Purif. Technol. 266, 118206. https://doi.org/10.1016/j.seppur.2020.118206

KYRIAKIDIS, Y.N., SILVA, D.O., BARROZO, M.A.S., VIEIRA, L.G.M., 2018. *Effect of variables related to the separation performance of a hydrocyclone with unprecedented geometric relationships*. Powder Technol. 338, 645–653. https://doi.org/10.1016/j.powtec.2018.07.064

LI, F., HUANG, G., ZOU, C., FU, Y., LI, J., MA, B., WANG, Y., ZHANG, C., 2025. *Numerical Analysis and Experimental Study on the Classification of Fine Particles Using a Hydrocyclone with Multiple Vortex Finders*. Separations 12, 318. https://doi.org/10.3390/separations12110318

LI, F., LIU, P., YANG, X., ZHANG, Y., JIANG, L., WANG, H., 2021a. *Numerical analysis of the effect of solid rod on the flow field and separation performance of thick-walled overflow pipe hydrocyclone*. Powder Technol. 388, 261–273. https://doi.org/10.1016/j.powtec.2021.04.077

LI, F., LIU, P., YANG, X., ZHANG, Y., LI, X., JIANG, L., WANG, H., FU, W., 2021b. *Numerical analysis on the effect of the length of arc-shaped vortex finder on the hydrocyclone's flow field and separation performance*. Miner. Eng. 172, 107172. https://doi.org/10.1016/j.mineng.2021.107172

LI, X., HAO, Y., LI, A., LIU, P., JIANG, L., CHEN, B., TIAN, S., 2026. *Experimental and numerical study on the hydrodynamics and classification performance of overflow adjustable hydrocyclones*. Powder Technol. 468, 121654. https://doi.org/10.1016/j.powtec.2025.121654

LI, X., LI, P., LI, F., GUO, D., 2025. *Improvement of separation performance of the hydrocyclone with dual enlarged outlets and an arc overflow tube*. Part. Sci. Technol. 43, 468–480. https://doi.org/10.1080/02726351.2025.2473521

LIU, P., FU, W., JIANG, L., YANG, X., ZHANG, Y., LI, X., ZHANG, Y., 2023. *Effect of the Position of Overflow Pipe*

with Mixed Spiral Structures on the Separation Performance of Hydrocyclones. Separations 10, 84. https://doi.org/10.3390/separations10020084

LIU, S., TAO, Y., XIE, N., TAO, L., HU, M., 2022. *Advance in grey system theory and applications in science and engineering*. Grey Syst. Theory Appl. 12, 804–823. https://doi.org/10.1108/GS-09-2021-0141

MARTÍNEZ, L.F., LAVÍN, A.G., MAHAMUD, M.M., BUENO, J.L., 2008. *Vortex finder optimum length in hydrocyclone separation.* Chem. Eng. Process. Process Intensif. 47, 192–199. https://doi.org/10.1016/j.cep.2007.03.003

PADHI, M., MANGADODDY, N., MAINZA, A.N., ANAND, M., 2021. *Study on the particle interaction in a hydrocyclone classifier with multi-component feed blend at a high solids content.* Powder Technol. 393, 380–396. https://doi.org/10.1016/j.powtec.2021.07.063

TAN, C., HU, H., YE, Q., E, D., CUI, J., ZHOU, Z., KUANG, S., ZOU, R., YU, A., 2024. *Multi-objective optimization of hydrocyclones using meta-heuristic algorithms and preference-informed decision-making*. Powder Technol. 444, 120050. https://doi.org/10.1016/j.powtec.2024.120050

TANG, B., XU, Y., SONG, X., SUN, Z., YU, J., 2015. *Numerical study on the relationship between high sharpness and configurations of the vortex finder of a hydrocyclone by central composite design.* Chem. Eng. J. 278, 504–516. https://doi.org/10.1016/j.cej.2014.11.022

TIAN, J., NI, L., SONG, T., OLSON, J., ZHAO, J., 2018. *An overview of operating parameters and conditions in hydrocyclones for enhanced separations.* Sep. Purif. Technol. 206, 268–285. https://doi.org/10.1016/j.seppur.2018.06.015

TOPRAK, N.A., ALTUN, O., 2021. *Considering hydrocyclone operation for tailings dewatering purpose and its effects on product specifications of paste backfill operations.* Miner. Eng. 173, 107176. https://doi.org/10.1016/j.mineng.2021.107176

ULLMANN, G., GONÇALVES, S.M., KYRIAKIDIS, Y.N., DE SOUZA BARROZO, M.A., VIEIRA, L.G.M., 2021. *Optimization study of thickener hydrocyclones.* Miner. Eng. 170, 107066. https://doi.org/10.1016/j.mineng.2021.107066

VAKAMALLA, T.R., KORUPROLU, V.B.R., ARUGONDA, R., MANGADODDY, N., 2017. *Development of novel hydrocyclone designs for improved fines classification using multiphase CFD model*. Sep. Purif. Technol. 175, 481–497. https://doi.org/10.1016/j.seppur.2016.10.026

VIEIRA, L.G.M., SILVA, D.O., BARROZO, M.A.S., 2016. E*ffect of Inlet Diameter on the Performance of a Filtering Hydrocyclone Separator.* Chem. Eng. Technol. 39, 1406–1412. https://doi.org/10.1002/ceat.201500724

WU, Z., LIANG, Z., LI, P., LI, F., YANG, H., 2025. *Effect of Vortex Finder Wall Thickness on Internal Flow Field and Classification Performance in a Hydrocyclone*. Separations 12, 149. https://doi.org/10.3390/separations12060149

ZHANG, T., LI, J., WEI, A., HUANG, J., LI, S., HUAN, J., WANG, F., WANG, H., 2023. *Ultra-clean separation of micro-particles in lubricant oil based on short-flow control of mini-hydrocyclone.* Sep. Purif. Technol. 304, 122370. https://doi.org/10.1016/j.seppur.2022.122370

ZHANG, W., HUANG, B., LI, Z., LAN, S., WANG, X., LIU, Q., YANG, X., 2024. *The effects of inlet diameter and feed particle concentration on hydrocyclone.* Int. J. Ambient Energy 45, 1–15. https://doi.org/10.1080/01430750.2024.2326650

ZHANG, Y., QIAN, P., LIU, Y., WANG, H., 2011. *Experimental Study of Hydrocyclone Flow Field with Different Feed Concentration.* Ind. Eng. Chem. Res. 50, 8176–8184. https://doi.org/10.1021/ie100210c

ZHANG, Y., XU, M., HU, W., XU, X., ZHANG, Q., 2023. *Vortex finder diameter and depth effects on the separation performance of hydrocyclone. Chem.* Eng. Res. Des. 195, 181–191. https://doi.org/10.1016/j.cherd.2023.05.052

ZHAO, Q., CUI, B., WEI, D., SONG, T., FENG, Y., 2019. *Numerical analysis of the flow field and separation performance in hydrocyclones with different vortex finder wall thickness.* Powder Technol. 345, 478–491. https://doi.org/10.1016/j.powtec.2019.01.030

ZHAO, Z., WANG, H., XIE, C., WEI, Y., XUE, J., XIAO, X., LIU, B., 2021. *Hydrocyclone separation performance influenced by feeding solid concentration and correcting separation size.* Heat Mass Transf. und Stoffuebertragung 57, 63–76. https://doi.org/10.1007/s00231-020-02940-8

Supplementary data

S1. Weighted grey relational analysis

Weighted grey relational analysis (GRA) was applied to the nine runs in the original $L_9(3^3)$ orthogonal experiment. Underflow yield, overflow fineness, and classification efficiency were treated as larger-the-better responses. The distinguishing coefficient was ρ = 0.5, and the respective weights were 0.30, 0.30, and 0.40. Each response was normalized by the larger-the-better min-max transformation:

$$x_i'(k) = \frac{x_i(k) - \min x(k)}{\max x(k) - \min x(k)} \quad \text{(S1)}$$

where $x_i(k)$ and $x'_i(k)$ are the original and normalized values of criterion k for run i, respectively. The ideal sequence was $x'_0(k)$ = (1, 1, 1), and the absolute deviation was:

$$\Delta_i k = |x_0'(k) - x_i'(k)| = |1 - x_i'(k)| \quad \text{(S2)}$$

The grey relational coefficient for each response was calculated as:

$$\xi_i(k) = \frac{\Delta_{min} + \rho\Delta_{max}}{\Delta_i(k) + \rho\Delta_{max}} \quad \text{(S3)}$$

where Δ_{min} = 0, Δ_{max} = 1, and ρ = 0.5.

The weighted grey relational grade was obtained from:

$$\gamma_i = \sum_{k-1}^{3} w_k \xi_i(k) \quad \text{(S4)}$$

where w_1 = 0.30, w_2 = 0.30, and w_3 = 0.40 correspond to underflow yield, overflow fineness, and classification efficiency, respectively. The runs were ranked in descending order of γ_i.

S2. Weight-sensitivity analysis

To examine the sensitivity to all three response weights, all nonnegative combinations of w_{UY}, w_{OF}, and w_{CE} were evaluated at intervals of 0.05, subject to $w_{UY} + w_{OF} + w_{CE} = 1$. This generated 231 weight combinations covering the complete weight simplex. For each combination, the grey relational grades and rankings were recalculated for both the original nine runs and the expanded dataset including the confirmation condition.

For the original dataset, Run 9 ranked first in 171 combinations (74.0%), whereas Run 1 ranked first in 60 combinations (26.0%). For the expanded dataset, Run 9 ranked first in 130 combinations (56.3%), whereas $A_1B_3C_3$ ranked first in 101 combinations (43.7%). The highest-ranked conditions across the complete weight domain are shown in Fig. S1.

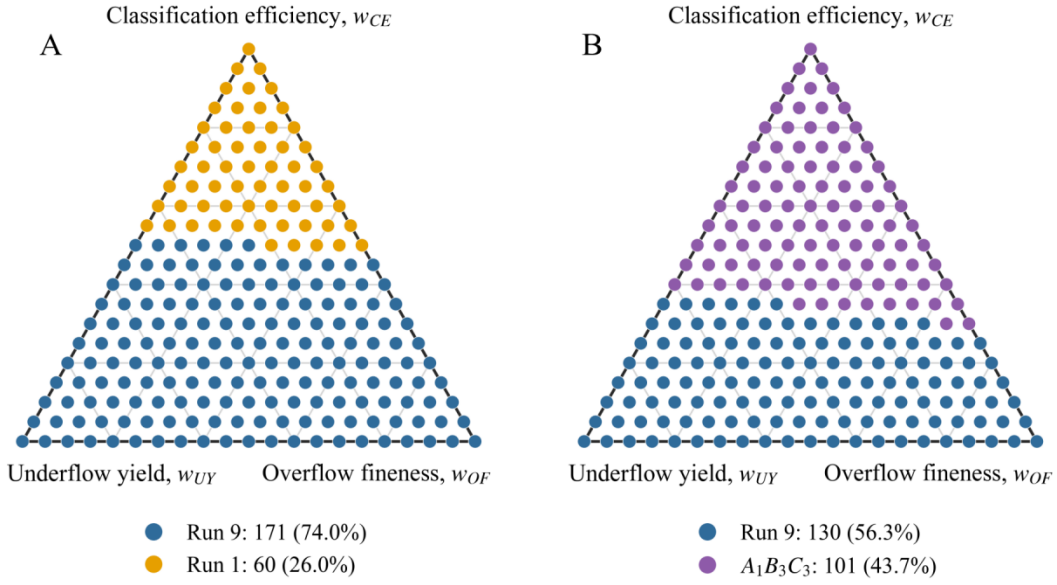


Fig. S1. Highest-ranked condition across the three-weight simplex for (A) the original nine runs and (B) the expanded dataset including the confirmation condition

S3. Confirmation experiment and expanded analysis

Main-effect analysis predicted $A_1B_3C_3$ as the preferred combination. The confirmation experiment produced an underflow yield of 58.62%, an overflow fineness of 88.91%, and a classification efficiency of 61.05%. The confirmation condition and the original nine runs were renormalized together using Eqs. (S1)–(S4) and the baseline weights. For the expanded validation, the minimum and maximum of each response were determined from the combined ten-condition dataset and then applied unchanged to all ten conditions. The original nine runs were re-ranked using this common scale to assess ranking stability, whereas the confirmation condition was assigned only an expanded rank. $A_1B_3C_3$ obtained the highest expanded grey relational grade (0.8040), followed by Run 9 (0.7482). It remained first for w_{CE} = 0.35–0.60, whereas Run 9 ranked first at w_{CE} = 0.30.

Table S1. Expanded grey relational grades and ranking stability of the original orthogonal runs before and after renormalization

Condition	Factor combination	Expanded GRG	Rank	Original rank	Re-normalized rank
Run 1	$A_1B_1C_1$	0.5244	3	2	2
Run 2	$A_1B_2C_3$	0.4367	6	5	5
Run 3	$A_1B_3C_2$	0.4750	4	4	3
Run 4	$A_2B_1C_3$	0.4128	8	7	7
Run 5	$A_2B_2C_2$	0.4624	5	3	4
Run 6	$A_2B_3C_1$	0.3500	9	8	8
Run 7	$A_3B_1C_2$	0.4311	7	6	6
Run 8	$A_3B_2C_1$	0.3468	10	9	9
Run 9	$A_3B_3C_3$	0.7482	2	1	1
Confirmation condition	$A_1B_3C_3$	0.8040	1	-	-